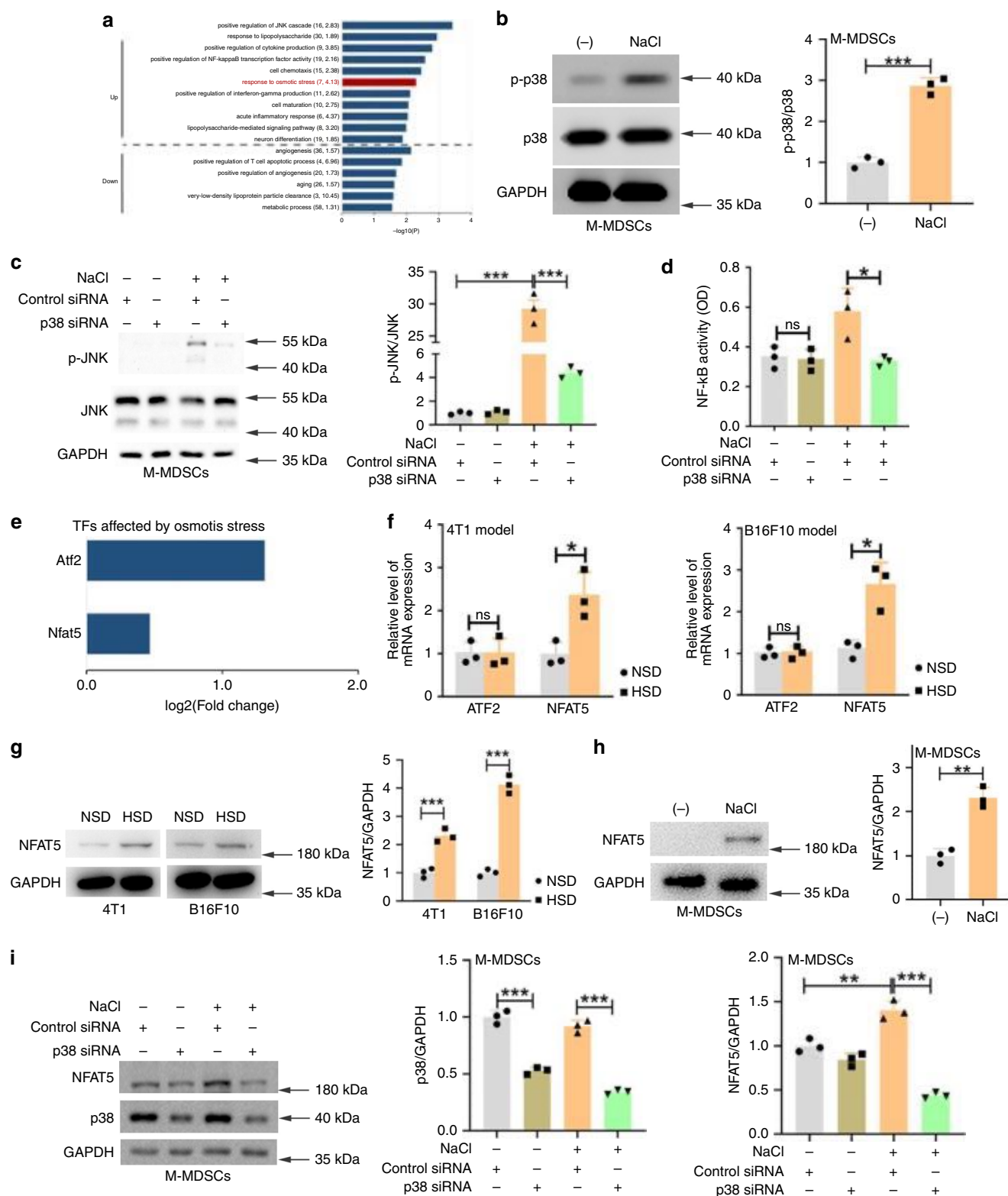


Fig. 6 Combined treatment with HSD and the anti-PD-1 antibody in tumour-bearing mice. **a–c** Female mice were subcutaneously implanted with 1×10^6 4T1 or B16F10 cells after starvation for 1 day and randomly assigned to receive the NSD or HSD for 16 days. On days 4, 8 and 12, mice were injected with 4 mg kg^{-1} control IgG antibody or 2 mg kg^{-1} anti-PD-1 via i.p. administration ($n = 10$ for each group). Images of tumours harvested from mice are shown, and tumour size was examined. Scale bar, 1 cm. **d–f** Tumours collected at day 16 were dissociated, and the proportions of CD4⁺ and CD8⁺ T cells in the CD45⁺ cell population were determined by flow cytometry. For all panels, $n = 10$ mice per group. One-way ANOVA with post hoc Bonferroni correction; * $p < 0.05$ and ** $p < 0.01$. Data are representative of three independent experiments. Data are presented as dot plots extending to minimum and maximum values in one independent experiment, and bars are presented as the mean \pm SEM of ten individual mice; each dot represents one mouse. Source data are provided as a Source Data file.

People in many countries currently consume a diet high in salt, sugar, fat and cholesterol, which has widespread implications in renal, cardiovascular and endocrine homeostasis, as well as cancer^{59,60}. Although some previous studies have shown that salt or salted food is involved in an increased risk of gastric cancer⁶¹, others have suggested little or only weak correlations^{60,62}. Furthermore, most conclusions have been obtained from epidemiologic studies. Little is known about the mechanism by which HSD can influence the initiation and promotion of cancer. Recently,

some studies have reported that HSD might stimulate the production of pro-inflammatory cytokines, such as TNF- α and IL-12, and inhibit the expression of IL-10 in vivo^{63,64}. Interestingly, these factors could also play a key role in preventing tumour growth by the immune system. This paradox might be due to the different requirements in cancer occurrence and development. Pro-inflammatory factors may contribute to cancer initiation by producing more DNA damage and a higher probability of mutations. After carcinogenesis, cancer development is usually



correlated with the immunosuppressive effects conveyed by the tumour cells and tumour microenvironment. In the present study, we used allograft cancer models to simulate a typical cancer developmental process. Based on our findings, the anticancer effect of HSD was derived from its significant reversal of the immunosuppression in cancer models via inhibiting MDSC activity or, possibly, other regulatory effects in other immune cells according to relevant studies.

Cancer immunotherapy represents a breakthrough in medicine. However, limitations exist as only a minority of patients respond to chimeric antigen receptor T-cell therapy or checkpoint inhibitors^{65,66}. Mounting evidence has shown that MDSCs represent a key obstacle for efficient cancer immunotherapy^{67,68}. Various strategies have therefore been sought to either alter MDSC function (such as cationic polymers⁶⁹ or entinostat³⁷) or eliminate MDSCs (such as doxorubicin¹⁶), abolish the

Fig. 7 HSD promoted the differentiation and function of M-MDSCs by p38/MAPK-dependent NFAT5 expression. **a** Significant Gene Ontology (GO) biological process terms associated with M-MDSCs from HSD-fed mice. Cellular processes enriched by the DEGs in M-MDSCs from 4T1 tumour-bearing HSD- or NSD-fed mice. The *p* value was tested by DAVID software using a hypergeometric test method. *n* = 5 mice for the NSD group and 6 mice for the HSD group. **b** Tumour M-MDSCs were stimulated with an additional 40 mM NaCl for 1 h, and phosphorylated p38 (p-p38) was analysed by western blotting. Right panels: quantification data. **c, d** Tumour M-MDSCs were transfected with p38-specific siRNA or control siRNA for 2 days, and cultured with an additional 40 mM NaCl for 24 h. Phosphorylated JNK (p-JNK) was analysed by western blotting (right panels: quantification data), and NF- κ B activity was determined by the p65 subunit DNA-binding ability. **e** Two TFs identified as upregulated DEGs in tumour M-MDSCs in 4T1 tumour-bearing HSD-fed mice. **f** ATF2 and NFAT5 mRNA level in tumour M-MDSCs in 4T1 or B16F10 tumour-bearing HSD- or NSD-fed mice was tested by qRT-PCR. **g** NFAT5 expression in M-MDSCs from tumour-bearing HSD- or NSD-fed mice was analysed by western blotting. Right panels: quantification data. **h** An equal number of tumour M-MDSCs were cultured for 24 h in the absence or presence of an additional 40 mM NaCl. NFAT5 expression was determined by western blotting. Right panels: quantification data. **i** Tumour M-MDSCs were transfected with p38-specific siRNA for 2 days, and cultured in the absence or presence of an additional 40 mM NaCl for 24 h. The level of NFAT5 was examined by western blotting. Right panels: quantification data. For **b–d** and **f–h**, two-tailed Student's *t* test; ns not significant; **p* < 0.05, ***p* < 0.01 and ****p* < 0.001; *n* = 5 mice for the NSD group and 6 mice for the HSD group. Bars are expressed as the means \pm SEM of 3 independent replicates with isolated cells pooled from the same group of mice. For **i**, *n* = 6 mice. ***p* < 0.01 and ****p* < 0.001. The data are expressed as the mean \pm SEM of independent three replicates; one-way ANOVA with post hoc Bonferroni correction. Experiments were repeated three times. Source data are provided as a Source Data file.

immunosuppression, restore immune surveillance and enhance the efficacy of cancer immunotherapy. Here, our data demonstrated that HSD partly relived the immunosuppression of MDSCs to enhance T-cell proliferation and function by promoting MDSC differentiation and changing their function, suggesting that HSD might enhance immunotherapies. Our study also demonstrated that, compared with monotherapy, the combination of HSD plus the anti-PD-1 antibody significantly decreased tumour growth by increasing T-cell infiltration. These findings might help to explain the differences in the response to cancer immunotherapy and benefit cancer immunotherapy by providing evidence supporting the integration of combinatorial therapeutic strategies.

Although our study is intriguing, whether HSD impacts the general health of animals still needs to be investigated. We found no marked changes in spleen, liver or kidney indexes, and no evidence of hepatotoxicity or nephrotoxicity; even body weight was unchanged by 16 days of high-salt intake, although HSD-fed mice consumed markedly more food and water than NSD-fed mice. In addition, our results were mainly based on transplanted tumours, indicating that HSD displays antitumour ability after tumour occurrence, but its role in tumorigenesis has been neglected. Therefore, whether HSD has antitumour activity in tumorigenesis needs to be investigated.

In summary, we demonstrated that HSD can restore anti-tumour immunosurveillance via regulating MDSC differentiation and function. We further identified a mechanism by which p38-dependent NFAT5 expression, secondary to high-salt exposure, was involved in mediating the differentiation of M-MDSCs into M1-type macrophages. Our findings indicate that HSD has an unexpected potential for immune regulation that may have further implications for cancer immunotherapy.

Methods

Cell lines. B16F10 (TCM36) and 4T1 (TCM32) cell lines were obtained from the Shanghai Cell Bank of Chinese Academy of Sciences (Shanghai, China). All cell lines were analysed for mycoplasma contamination using a mycoplasma stain assay kit (Beyotime Biotechnology, Shanghai, China). All cell lines were cultured in RPMI-1640 or DMEM supplemented with 10% heat-inactivated foetal bovine serum (FBS), 100 U ml⁻¹ penicillin and 0.1 mg ml⁻¹ streptomycin.

Protein and qRT-PCR. For western blotting analyses, cells were homogenised in RIPA buffer (Beyotime Biotechnology, Shanghai, China). After the samples were mixed with 2 \times Laemmli buffer and boiled for 5 min, 50 μ g of each protein were subjected to sodium dodecyl sulfate polyacrylamide gel electrophoresis and transferred onto polyvinylidene fluoride membranes (Millipore, Bedford, MA, USA) using Semi-Dry Trans-Blot (Bio-Rad Laboratories). Immunoblots were first incubated in 5% nonfat dry milk for 1 h at room temperature (RT) and then incubated with the indicated primary antibodies at appropriate dilutions overnight at 4 °C. Subsequently, immunoblots were washed with PBS Tween, incubated with horseradish

peroxidase-conjugated anti-rabbit immunoglobulin G (CST, Danvers, MA, USA; 7074 S) for 60 min at RT and detected using an enhanced chemiluminescence system (Millipore, Billerica, MA, USA) by Tanon 4200SF Gel Imaging System (Shanghai, China). The protein bands were quantitated by densitometry using ImageJ software (NIH, Bethesda, MD). Information regarding the antibodies used is listed in Supplementary Table 1. The pre-stained Protein Ladder (26616 or 26634, Thermo Scientific) was used as size standards in western blotting. All blots and gels are accompanied by the locations of molecular weight/size markers, which, together with uncropped and unprocessed scans of the most important blots (Figs. 7h and 8h, Supplementary Figs. 14a and 16b), are provided in combined source data.

For qRT-PCR analyses, total RNA was extracted by TRIzol reagent (Invitrogen, Carlsbad, CA, USA) according to the manufacturer's instructions, and 500 ng of RNA was converted to cDNA using PrimeScriptTM RT Master Mix (Perfect Real Time) (Takara, Da Lian, China). qRT-PCR assays to test the differences in mRNA expression were performed on a 7300 Sequence Detection System (Applied Biosystems, Foster City, CA, USA) using EvaGreen Dye (Biotium, Hayward, CA, USA). mRNA expression was normalised to the expression of β -actin. Transcript levels were calculated relative to the levels of the internal control β -actin, and are expressed as $2^{-\Delta\Delta CT}$, in which $\Delta\Delta CT = C_{T, \text{mRNA}} - C_{T, \beta\text{-actin}}$. The gene-specific primers used can be found in Supplementary Table 2.

RNA interference. Mouse NFAT5 siRNA (sense: 5'-GGUACAGCCUGAAAC CCAATT-3' and antisense: 5'-UUGGGUUUCAGGCUGUACCTT-3') was obtained from Gene-Pharm (Shanghai, China). p38 MAPK siRNA (CST#6564) was purchased from Cell Signalling Technology (Danvers, MA, USA). Electroporation was performed using a Gene Pulser electroporation (Bio-Rad, Hercules, USA) and a 0.1-cm electrode gap cuvette (Bio-Rad). The electroporated cells were maintained at 37 °C for 20 min, and then transferred into six-well plates. The treatments were performed 24 h after siRNA transfection.

Microarray analysis. The RNA extracts were first evaluated by a Nanodrop ND-1000 spectrophotometer (Thermo Fisher Scientific, Waltham, MA), and RNA quality was determined by the ratios of A260/A280 (close to 2) and A260/A230 (close to 2). Microarray analysis of the genome-wide expression profile was done by KangChen Biotech (Shanghai, China) with the Agilent Mouse GE v2 Microarrays (4 \times 44 k format) (Agilent Technologies).

Animals and tumour models. Female and male C57BL/6J and BALB/C mice (6–8 weeks old) and female BABL/C-*nu/nu* mice (6–8 weeks old) were obtained from the Animal Centre of Yangzhou University (Yangzhou, China), and the permission number is SCXX(su)2017-007. Mice were maintained under a 12-h light/12-h dark cycle in specific pathogen-free (SPF) conditions at 22–24 °C. All mice were fed normal chow diets (for C57BL/6J and BALB/C mice, rodent diet, 1010041, Shooobree, Xietong Organism, Jiangsu, China; for BABL/C-*nu/nu* mice, rodent diet, 1010019, Shooobree, Xietong Organism, Jiangsu, China) and water ad libitum, and were treated in strict accordance with the Nanjing University guidelines (Permit NO. 2011-039) and the ARRIVE guidelines (Animal Research: Reporting of In Vivo Experiments).

To generate the heterotopic tumour model, mice were subcutaneously injected with 1×10^6 cells (B16F10 or 4T1) after 1 day of starvation. The cells were injected into the left armpit of each mouse. Then, mice were randomly assigned to receive the NSD (0.4% NaCl in chow plus tap water) or HSD (4% NaCl in chow plus 1% NaCl in the water) via random lottery for 16 days (10 mice per group). We tested the tumour size with callipers and weighed the tumour samples upon harvest. The main ingredients and caloric content in NSD and HSD are listed in Supplementary Table 3.

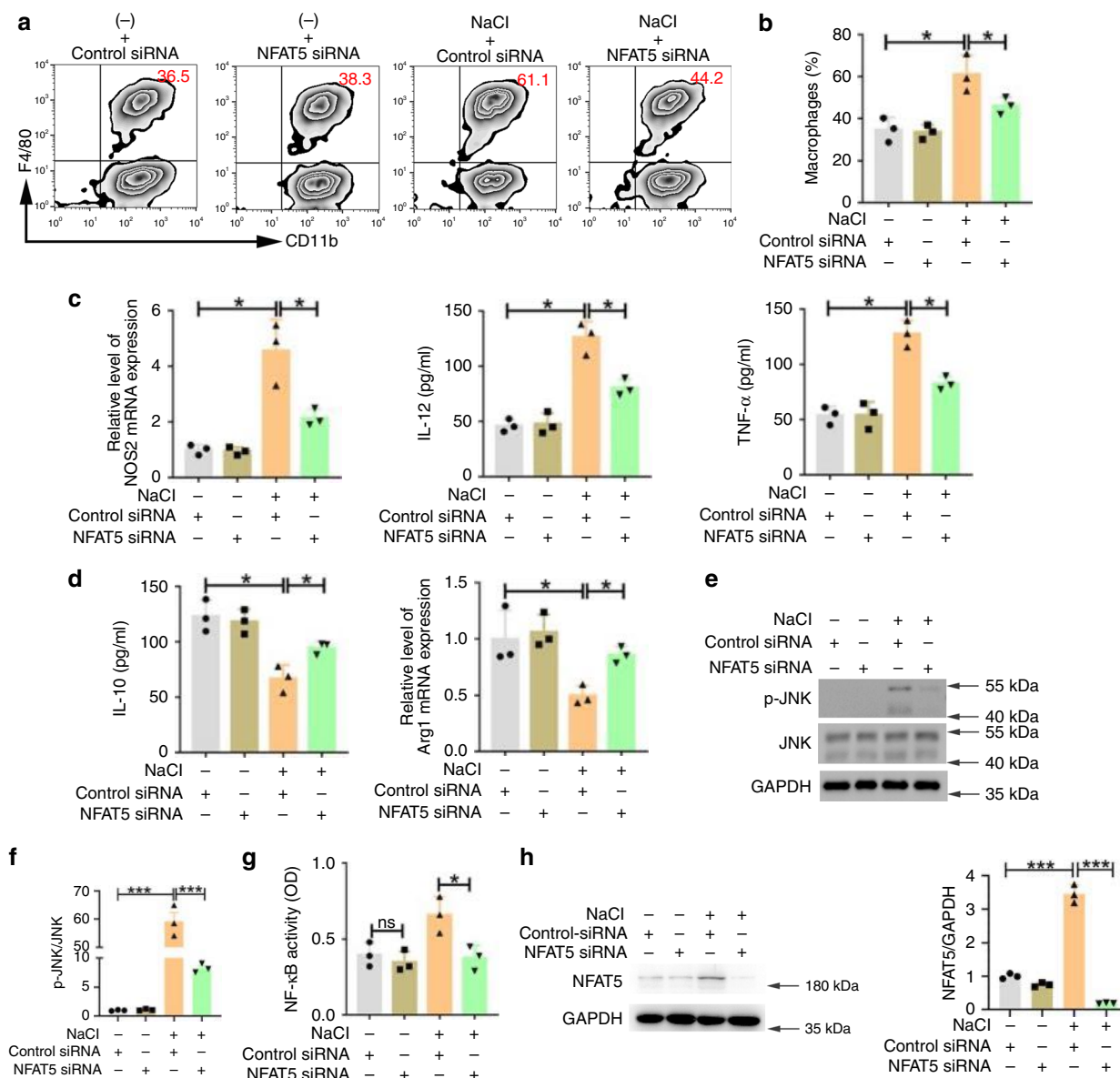


Fig. 8 NFAT5 silencing inhibited high-salt-mediated M-MDSC differentiation and functional transformation. **a, b** Purified tumour M-MDSCs were transfected with NFAT5-specific siRNA and cultured in the absence or presence of an additional 40 mM NaCl for 3 days. Populations of CD11b⁺F4/80⁺ cells were tested by flow cytometry. **c, d** Purified tumour M-MDSCs were transfected with NFAT5-specific siRNA for 2 days and cultured in the absence or presence of an additional 40 mM NaCl for 24 h. The expression of IL-12, TNF-α and IL-10 in the supernatant was determined by ELISA. NOS2 and Arg1 mRNA expression levels were evaluated by qRT-PCR. **e–g** p-JNK was analysed by western blotting; quantification data of western blotting and NF-κB activity were determined by the p65 subunit DNA-binding ability. **h** NFAT5 expression was analysed by western blotting. Right panels: quantification data. For all panels, **p* < 0.05 and ****p* < 0.001. Bars are expressed as the means ± SEM of three independent replicates with isolated pooled cells. These experiments were repeated three times and were replicated with similar results; *n* = 5 mice; one-way ANOVA with post hoc Bonferroni correction. Source data are provided as a Source Data file.

For the analysis of the effect of HSD on food and water intake and mouse body weight, mice were first randomly assigned to two groups via random lottery, the tumour-free group and tumour group. Mice in the tumour group were subcutaneously injected with 1×10^6 cells (B16F10 or 4T1) into the left armpit after 1 day of starvation. Then, mice were randomly assigned to four groups (10 mice per group): NSD + tumour-free group (NSD group), HSD + tumour-free group (HSD group), NSD + tumour group (NSD + tumour group) or HSD + tumour group (HSD + tumour group). Mice received the NSD or HSD for 16 days. On days 4, 8, 12 and 16, the food and water intake of mice were tested, and the changes in the body weights of mice were tested every 4 days.

For the analysis of the effect of HSD on the general health of the animals, mice were randomly assigned to receive an NSD or HSD via random lottery for 16 days (10 mice per group). At day 16, different tissues were harvested and weighed. After the blood samples clotted for 1 h at RT, they were centrifuged at $835 \times g$ for 15 min for serum collection. Animal serum ALT, AST, BUN and creatinine levels were

examined for the evaluation of liver and kidney function, according to the manufacturer's instructions. The ALT assay kit (C009-2), AST assay kit (C010-2), urea assay kit (C013-2) and creatinine assay kit (sarcosine oxidase, C011-2) were purchased from Nanjing Jiancheng Bioengineering Institute (Nanjing, China).

For the analysis of the effect of the combination of HSD and anti-PD-1 treatment in the subcutaneously implanted tumour models, mice were subcutaneously injected with 1×10^6 cells (B16F10 or 4T1) into the left armpit after 1 day of starvation, and then randomly assigned to four groups (10 mice per group) via random lottery: the NSD group, HSD group, anti-PD-1 antibody group or combined HSD and anti-PD-1 antibody groups. Mice were fed the NSD or HSD for 16 days. On days 4, 8 and 12, mice were injected with 4 mg kg^{-1} isotype controls (clone 2A3, Bioxell, West Lebanon, NH) or 2 mg kg^{-1} anti-PD-1 antibody (clone RMP1-14, Bioxcell) via intraperitoneal (i.p.) administration. At day 16, we measured tumour size with callipers and weighed the tumour samples upon harvest.

For the analysis of the effect of the combination of HSD and angiotensin-converting enzyme inhibitor (captopril) treatment in the subcutaneous implantation tumour model, mice were subcutaneously injected with 1×10^6 cells (B16F10 or 4T1) into the left armpit after 1 day of starvation. Then, mice were randomly assigned to four groups (6 mice per group) via random lottery: the NSD group, HSD group, captopril group or combined HSD and captopril groups. Mice were fed the NSD or HSD for 16 days. Meanwhile, mice in the captopril group received captopril ($10 \text{ mg kg}^{-1} \text{ d}^{-1}$) by gavage every day. At day 16, we measured tumour size with callipers and weighed the tumour samples upon harvest. Captopril was purchased from Dalian Meilun Biotech Co., Ltd. (Dalian, China).

For the analysis of the effect of NFAT5 on HSD-mediated differentiation of M-MDSCs into macrophages *in vivo*, mice were subcutaneously injected with 1×10^6 cells (B16F10 or 4T1) into the left armpit after 1 day of starvation and randomly assigned to four groups (6 mice per group) via random lottery: the NSD group, HSD group, NFAT5 siRNA-LV group or the combined HSD and NFAT5 siRNA-LV groups. Mice were fed the NSD or HSD for 16 days. Meanwhile, mice were administered with lentivirus carrying NFAT5 siRNA under the *Ly-6C* promoter (NFAT5 siRNA-LV, GenePharma Company, Shanghai, China) via the tail vein (10^9 PFU per mouse) every 2 days. At day 16, we measured tumour size with callipers and weighed the tumour samples upon harvest.

For the analysis of the effect of HSD after MDSC depletion in the subcutaneously implanted tumour models, mice were subcutaneously injected with 1×10^6 cells (B16F10 or 4T1) into the left armpit after 1 day of starvation and then randomly assigned to three groups (10 mice per group) via random lottery: the NSD group, HSD group or combined HSD and anti-Gr-1 antibody groups. Mice were fed the NSD or HSD for 16 days. Mice were injected with $200 \mu\text{g}$ of isotype controls (clone LTF-2, Bioxell, West Lebanon, NH) or $200 \mu\text{g}$ of anti-Gr-1 monoclonal antibody (clone RB6.8C5, Bioxcell) via intraperitoneal (i.p.) administration every 2 days. At day 16, we measured tumour size with callipers and weighed the tumour samples upon harvest.

All *in vivo* experiments were conducted by using a double-blind manner so that the group identity for each tumour-bearing mice was not disclosed to the scientists until all results were completed. All mice were adapted to the laboratory for 7 days to observe the health status. The mice were weighed when used in experiments (Supplementary Fig. 2c), and mice could be excluded from the experiment with rapid weight loss or infection during the progression of the experiment. Mice were killed via cervical dislocation after completing all animal experiments.

Histological and immunofluorescence analysis. After tumour tissues were fixed with 4% paraformaldehyde, they were embedded in paraffin and sectioned. The sections were de-paraffinised in xylene and rehydrated in graded alcohol. For histologic analyses, the sections were counterstained with haematoxylin and eosin (H&E), and the tumour necrotic area per field was quantified using ImageJ software (NIH). For immunofluorescence analyses for tumour tissues, after antigen retrieval by boiling sections in citrate antigen retrieval solution (Beyotime Biotechnology, Shanghai, China) for 10 min, the sections were blocked with 5% bovine serum albumin (BSA) for 1 h and incubated with primary antibodies at 4°C overnight. The slices were washed and incubated for 1 h with fluorescence-conjugated secondary antibodies. For immunofluorescent analyses for T cells, isolated CD4^+ T cells and CD8^+ T cells were fixed with 4% paraformaldehyde for 15 min, penetrated with 0.3% Triton X-100 for 10 min, blocked with 3% BSA for 30 min and stained with primary antibodies for 2 h at RT. Cells were washed and incubated for 1 h with fluorescence-conjugated secondary antibodies. Finally, the nuclei were stained with DAPI (Beyotime Biotechnology, Shanghai, China) and coverslipped. Sections were examined using a Nikon confocal microscope, and each immunofluorescent stain was repeated three times using serial sections. The number of double-positive cells and vessels per field was quantified using ImageJ software. The quantitation of double-positive cells and vessels per field was conducted by using a single-blind manner so that the section identity for different groups was not disclosed to the scientists until all results were completed. Information regarding the antibodies used is listed in Supplementary Table 1.

Cell flow cytometry. Cell suspensions from the blood, spleen or tumour tissues were filtered through Nylon cell strainers ($70 \mu\text{m}$, Falcon, USA), and red blood cells (RBCs) were lysed. After cells were washed with phosphate-buffered saline (PBS) containing 1% BSA, cells were blocked with 1% BSA at 4°C for 30 min. For extracellular staining, 7-AAD was used for live/dead cell determination. For intracellular staining, Fixability viability Dye 520 (FVD eFluor 520, eBioscience) was used for live/dead cell determination. For extracellular staining, 1×10^6 cells were incubated with antibodies for 30 min on ice and then washed with 1% BSA. For intracellular staining, cells were first stained on ice for 30 min with surface-staining antibodies, washed, fixed and permeabilised with the FIX&PERM Kit (Multi Sciences, GAS003) and stained with cytokine antibodies. For analysis of Tregs, Tregs were assayed by the Mouse Regulatory T cell Staining Kit (Multi Sciences, KTR201-100) according to the manufacturer's recommendation. The samples were resuspended in $500 \mu\text{l}$ of 1% BSA and analysed by flow cytometry. Flow cytometry was performed on a FACSCalibur device (Becton-Dickinson, Mountain View, CA, USA), and the data were evaluated with FlowJo v10.0 software (Tree Star). The proportions of immune cells examined by flow cytometry were conducted by using a single-blind manner so that the flow cytometry data identity

for different groups was not disclosed to the scientists until all results were completed. Information regarding the antibodies used is listed in Supplementary Table 4.

Cytokine antibody array and ELISA. Tumour-bearing mice were fed the HSD or NSD for 16 days. Tumour tissue was then homogenised in PBS containing protease inhibitors. After homogenisation, Triton X-100 was added to the tumour homogenates (at a final concentration of 1%), which were then thawed, frozen at -80°C for 1 day and centrifuged at $13,362 \times g$ for 30 min at 4°C to remove cellular debris. After protein quantitation using a BCA protein assay kit, $400 \mu\text{g}$ of tumour homogenates from both the NSD and HSD groups were used. Blood samples were obtained from mice in each cohort and allowed to clot for 1 h at RT before centrifuging for 15 min at $835 \times g$ rpm. Serum samples were harvested and mixed at equal volumes. The mixed homogenates and serum were assayed by the Proteome Profiler Mouse XL Cytokine Array (ARY028, R&D Systems, Inc.) according to the manufacturer's recommendation. Briefly, the membranes were blocked with the blocking buffer (Array Buffer) at RT for 1 h and incubated with the samples ($200 \mu\text{l}$ of serum or $200 \mu\text{g}$ of tumour lysates) at 4°C overnight. Membranes were washed three times with Wash Buffer at RT for 10 min per wash and incubated with biotin-conjugated antibodies at RT for 1 h. Next, the membranes were washed and incubated with horseradish peroxidase-conjugated streptavidin at RT for 30 min. After the membranes were washed three times with wash buffer, the membranes were incubated with detection buffer for 1 min. We used a luminescence detector (Chemi Scope 6300, CSI, Shanghai, China) for detection, and the results were digitised and subjected to image analysis (ImageJ, freely downloaded from the National Institutes of Health website, <http://rsbweb.nih.gov/ij/>). We obtained the relative protein concentrations by subtracting the background staining and normalising to the positive controls on the same membrane. The complete list of multiple cytokines, chemokines, growth factors and other soluble proteins in Proteome Profiler Mouse XL Cytokine Array is displayed in Supplementary Table 5.

For ELISA, the TNF- α , IL-12, INF- γ , ICAM-1, IL-6, GM-CSF, IL-10 and PGE2 concentration in serum, tissue lysates or cell supernatant was tested by using ELISA kits (4A Biotech Co., Ltd., Beijing, China), according to the manufacturer's instructions.

MDSC isolation. Total MDSCs (T-MDSCs, $\text{CD11b}^+\text{Gr-1}^+$), M-MDSCs ($\text{CD11b}^+\text{Ly6-C}^+$) and PMN-MDSCs ($\text{CD11b}^+\text{Ly6-G}^+$) were isolated from the tumour tissues by the Myeloid-Derived Suppressor Cell Isolation Kit according to the manufacturer's instructions (Miltenyi Biotec, Bergisch Gladbach, Germany), with all steps performed at 4°C . Briefly, tumour-bearing mice fed the NSD or HSD for 16 days were sacrificed, and tumour tissues were harvested. Fresh tumour tissues were cut into pieces and then enzymatically digested with 0.2% collagenase IV (weight per volume) and 0.1% DNase (wt per vol) (Sangon Biotech, China) for 1 h at 37°C . After the cells were filtered through $70 \mu\text{m}$ Nylon cell strainers (Falcon, USA), the resulting cell suspension was centrifuged at $93 \times g$ for 5 min. The cells were depleted of RBCs using RBC lysis buffer and washed twice with cold PBS containing 1% BSA. After treatment with FcR blocking reagent ($50 \mu\text{l}$ per 10^8 cells) for 10 min, cells were stained with the biotin-conjugated granulocyte receptor (GR)-1 or Ly-6G monoclonal antibody and further labelled with anti-biotin or streptavidin microbeads. Then, cells were passed through the MACS column (MS or LS separation column) for magnetic cell separation. The retained cells were M-MDSCs or PMN-MDSCs, and the purity and cell viability of the MDSC subfractions were typically greater than 90% (Supplementary Fig. 20a, b).

Macrophage, T-cell isolation from tumour tissues. Fresh tumour tissues were prepared as single-cell suspensions, minced in the DMEM with 0.2% collagenase IV (weight per volume) and 0.1% DNase (wt per vol) for 1 h at 37°C and filtered through $70 \mu\text{m}$ Nylon cell strainers (Falcon, USA). F4/80^+ cells, CD4^+ T cells and CD8^+ T cells were isolated from single-cell suspensions by anti-F4/80 microbeads ultrapure mouse (130-110-443, Miltenyi Biotec), Anti-Mouse CD4—DM (551539, BD) and Anti-Mouse CD8a Particles—DM (551516, BD) according to the manufacturer's instructions, with all steps performed at 4°C .

M-MDSC and monocyte differentiation. For M-MDSC differentiation experiments, freshly isolated tumour M-MDSCs from tumour tissues from the NSD and HSD groups were cultured in RPMI-1640 medium supplemented with 10% FBS and 10 ng ml^{-1} GM-CSF (Peprotech) for 2, 3 and 4 days. For normal monocyte differentiation, monocytes were isolated from blood using a mouse peripheral monocyte separation medium kit according to the manufacturer's protocol (TBD, TBM2011M). Isolated monocytes were cultured in RPMI-1640 medium supplemented with 10% FBS, 10 ng ml^{-1} GM-CSF (Peprotech) and an additional 40 mM of NaCl for 3 days. $\text{CD11b}^+\text{F4/80}^+$ cells were analysed by flow cytometry.

Cell viability assay. During M-MDSC differentiation, 1×10^6 cells were collected and resuspended in $500 \mu\text{l}$ of 1% BSA. Then, cells were stained with $5 \mu\text{l}$ of 7-aminoactinomycin-D (7-AAD). After 10 min, cells were analysed by flow cytometry.

T-cell proliferation assay. Total spleen cells from healthy mice were stained with carboxyfluorescein succinimidyl ester (CFSE, Beyotime) at 2.5 μ M and cultured with PMN-MDSCs isolated from tumour tissues from different groups in a 96-well plate. Spleen cells were co-cultured with PMN-MDSCs at a 2:1 ratio. These cells were stimulated with Con A (2 μ g ml⁻¹, Sigma-Aldrich, New Jersey, USA) and left in culture for 3 days before being analysed by flow cytometry.

ROS detection. PMN-MDSCs isolated from tumour tissues from NSD- or HSD-fed mice were incubated with dichlorofluorescein diacetate (DCFH-DA, ROS Assay Kit, Beyotime Biotechnology, Shanghai, China) for 30 min at 37 °C. Cells were then stained with anti-Ly-6G antibodies. The level of ROS was tested using flow cytometry as described.

NF- κ B (p65) activity assay. Nuclear extracts from M-MDSCs were prepared using a nuclear extract kit (Cayman Chemical, #10009277, Ann Arbor, MI, USA). The nuclear extracts were adjusted to the same protein concentration by a BCA protein assay kit, and then the DNA-binding activity of NF- κ B was examined using a NF- κ B (p65) TF assay kit (Cayman Chemical, #10007889) according to the manufacturer's instructions.

Chemical analysis of tissue electrolyte and water content. Thymus, liver, spleen, heart, lung and tumour tissues isolated from the NSD and HSD groups were weighed (wet weight), frozen at -80 °C for 24 h and then freeze-dried using a Labconco FreeZone 2.5 L freeze dryer (Table Model, USA) for 48 h (dry weight [DW]). The difference between the wet weight and DW was tissue water content. We then put the tissues in 50% HNO₃ for 48 h and incubated them at 190 °C for 12 h. Finally, we dissolved the tissues in 1% HNO₃ and examined Na⁺ and K⁺ content by atomic adsorption spectrometry (HITACHI180-80) and Cl⁻ content by titration with 0.1 N silver nitrate (Model Titrand, German Metrohm).

X-ray fluorescence spectrometry analysis. Tumours isolated from the NSD and HSD groups were frozen at -80 °C for 24 h and then desiccated in a freeze dryer for 48 h. The Na⁺, K⁺ and Cl⁻ content of tumour samples was assayed by X-ray fluorescence spectrometry at the Center of Modern Analysis (Nanjing University).

Osmolality measurements. Tissue osmolality was examined by using a vapour-pressure osmometer (Vapro 5520, Wescor, Logan, UT) as previously reported⁴³. Briefly, tissue obtained from anaesthetised NSD- or HSD-fed mice was placed in a 1.5-ml tube and snap-frozen by dry ice. Tissue fluid from frozen tissue that had been fragmented was added into filter discs and osmolality was measured. The whole-blood osmolality measurements were identical to those of serum, which was measured by a STY-1A pressure osmometer (TDTF, Tianjing, China).

Statistical analysis. All data are presented as the mean \pm standard error. Data visualisation and statistical analysis were performed using Prism 5 or 7 (GraphPad Software Inc., La Jolla, CA, USA), after all the data sets for normal distribution were tested by IBM SPSS Statistics 20 software (IBM Corp., Armonk, NY, USA). Differences between two groups were evaluated using the two-tailed Student's *t* test or the two-tailed Wilcoxon rank-sum tests. Differences between multiple groups were compared using one-way ANOVA with post hoc Bonferroni correction or one-way ANOVA with Dunnett's test. Details of statistical analyses including sample numbers (*n*) are included in the respective figure legends. NS indicates not statistically significant, and the difference was considered significant when *p* < 0.05. At last, the results and relevant accuracy about all in vivo experiments are provided in figures and figure legends.

Reporting summary. Further information on research design is available in the Nature Research Reporting Summary linked to this article.

Data availability

All relevant data are available in the article, Supplementary Information or from the corresponding author upon request. The source data underlying all figures are provided as a Source Data file. The microarray data have been deposited in the Gene Expression Omnibus (GEO)/NCBI public database (accession no. GSE125430, <https://www.ncbi.nlm.nih.gov/geo/query/acc.cgi?acc=GSE125430>).

Received: 11 June 2018; Accepted: 12 March 2020;
Published online: 07 April 2020

References

- Jiang, X. et al. High sodium chloride consumption enhances the effects of smoking but does not interact with SGK1 polymorphisms in the development of ACPA-positive status in patients with RA. *Ann. Rheum. Dis.* **75**, 943–946 (2016).
- Mozaffarian, D. et al. Global sodium consumption and death from cardiovascular causes. *N. Engl. J. Med.* **371**, 624–634 (2014).
- Kleinewietfeld, M. et al. Sodium chloride drives autoimmune disease by the induction of pathogenic TH17 cells. *Nature* **496**, 518–522 (2013).
- Brown, I. J., Tzoulaki, I., Candeias, V. & Elliott, P. Salt intakes around the world: implications for public health. *Int. J. Epidemiol.* **38**, 791–813 (2009).
- Faraco, G. et al. Dietary salt promotes neurovascular and cognitive dysfunction through a gut-initiated TH17 response. *Nat. Neurosci.* **21**, 240–249 (2018).
- Wu, C. et al. Induction of pathogenic TH17 cells by inducible salt-sensing kinase SGK1. *Nature* **496**, 513–517 (2013).
- Hernandez, A. L. et al. Sodium chloride inhibits the suppressive function of FOXP3+ regulatory T cells. *J. Clin. Invest.* **125**, 4212–4222 (2015).
- Binger, K. J. et al. High salt reduces the activation of IL-4- and IL-13-stimulated macrophages. *J. Clin. Invest.* **125**, 4223–4238 (2015).
- Ip, W. K. & Medzhitov, R. Macrophages monitor tissue osmolality and induce inflammatory response through NLRP3 and NLR4 inflammasome activation. *Nat. Commun.* **6**, 6931 (2015).
- Hucke, S. et al. Sodium chloride promotes pro-inflammatory macrophage polarization thereby aggravating CNS autoimmunity. *J. Autoimmun.* **67**, 90–101 (2016).
- Sigaux, J., Semerano, L., Favre, G., Bessis, N. & Boissier, M. C. Salt, inflammatory joint disease, and autoimmunity. *Joint Bone Spine* **85**, 411–416 (2018).
- Tubbs, A. L., Liu, B., Rogers, T. D., Sartor, R. B. & Miao, E. A. Dietary salt exacerbates experimental colitis. *J. Immunol.* **199**, 1051–1059 (2017).
- Sundstrom, B., Johansson, I. & Rantapaa-Dahlqvist, S. Interaction between dietary sodium and smoking increases the risk for rheumatoid arthritis: results from a nested case-control study. *Rheumatology* **54**, 487–493 (2015).
- Ouzounova, M. et al. Monocytic and granulocytic myeloid derived suppressor cells differentially regulate spatiotemporal tumour plasticity during metastatic cascade. *Nat. Commun.* **8**, 14979 (2017).
- Bauer, R. et al. Blockade of myeloid-derived suppressor cell expansion with all-trans retinoic acid increases the efficacy of antiangiogenic therapy. *Cancer Res.* **78**, 3220–3232 (2018).
- Alizadeh, D. et al. Doxorubicin eliminates myeloid-derived suppressor cells and enhances the efficacy of adoptive T-cell transfer in breast cancer. *Cancer Res.* **74**, 104–118 (2014).
- Taki, M. et al. Snail promotes ovarian cancer progression by recruiting myeloid-derived suppressor cells via CXCR2 ligand upregulation. *Nat. Commun.* **9**, 1685 (2018).
- Kumar, V. et al. CD45 phosphatase inhibits STAT3 transcription factor activity in myeloid cells and promotes tumor-associated macrophage differentiation. *Immunity* **44**, 303–315 (2016).
- Gabrilovich, D. I. & Nagaraj, S. Myeloid-derived suppressor cells as regulators of the immune system. *Nat. Rev. Immunol.* **9**, 162–174 (2009).
- Ben-Meir, K., Twaik, N. & Baniyash, M. Plasticity and biological diversity of myeloid derived suppressor cells. *Curr. Opin. Immunol.* **51**, 154–161 (2018).
- Kumar, V., Patel, S., Tcyganov, E. & Gabrilovich, D. I. The nature of myeloid-derived suppressor cells in the tumor microenvironment. *Trends Immunol.* **37**, 208–220 (2016).
- Liu, G. et al. SIRT1 limits the function and fate of myeloid-derived suppressor cells in tumors by orchestrating HIF-1 α -dependent glycolysis. *Cancer Res.* **74**, 727–737 (2014).
- Ma, G. et al. Paired immunoglobulin-like receptor-B regulates the suppressive function and fate of myeloid-derived suppressor cells. *Immunity* **34**, 385–395 (2011).
- Fridlender, Z. G. et al. Polarization of tumor-associated neutrophil phenotype by TGF- β : “N1” versus “N2” TAN. *Cancer Cell* **16**, 183–194 (2009).
- Jantsch, J. et al. Cutaneous Na⁺ storage strengthens the antimicrobial barrier function of the skin and boosts macrophage-driven host defense. *Cell Metab.* **21**, 493–501 (2015).
- Tellechea, M., Buxade, M., Tejedor, S., Aramburu, J. & Lopez-Rodriguez, C. NFAT5-regulated macrophage polarization supports the proinflammatory function of macrophages and T lymphocytes. *J. Immunol.* **200**, 305–315 (2018).
- Choi, S. et al. Transcription factor NFAT5 promotes macrophage survival in rheumatoid arthritis. *J. Clin. Invest.* **127**, 954–969 (2017).
- Willebrand, R. et al. High salt inhibits tumor growth by enhancing anti-tumor immunity. *Front. Immunol.* **10**, 1141 (2019).
- Lin, Y. et al. Chemerin has a protective role in hepatocellular carcinoma by inhibiting the expression of IL-6 and GM-CSF and MDSC accumulation. *Oncogene* **36**, 3599–3608 (2017).
- Bayne, L. J. et al. Tumor-derived granulocyte-macrophage colony-stimulating factor regulates myeloid inflammation and T cell immunity in pancreatic cancer. *Cancer Cell* **21**, 822–835 (2012).
- Pinter, M. & Jain, R. K. Targeting the renin-angiotensin system to improve cancer treatment: implications for immunotherapy. *Sci. Transl. Med.* **9**, 1–11 (2017).

32. Drenjancevic-Peric, I. et al. High-salt diet and hypertension: focus on the renin-angiotensin system. *Kidney Blood Press. Res.* **34**, 1–11 (2011).
33. Li, W. et al. Aerobic glycolysis controls myeloid-derived suppressor cells and tumor immunity via a specific CEBPB isoform in triple-negative breast cancer. *Cell Metab.* **28**, 87–103 e106 (2018).
34. Cheng, W. F. et al. Tumor-specific immunity and antiangiogenesis generated by a DNA vaccine encoding calreticulin linked to a tumor antigen. *J. Clin. Invest.* **108**, 669–678 (2001).
35. Zhou, L. et al. HOXA9 inhibits HIF-1 α -mediated glycolysis through interacting with CRIP2 to repress cutaneous squamous cell carcinoma development. *Nat. Commun.* **9**, 1480 (2018).
36. Chiu, D. K. et al. Hypoxia inducible factor HIF-1 promotes myeloid-derived suppressor cells accumulation through ENTPD2/CD39L1 in hepatocellular carcinoma. *Nat. Commun.* **8**, 517 (2017).
37. Orillion, A. et al. Entinostat neutralizes myeloid-derived suppressor cells and enhances the antitumor effect of PD-1 inhibition in murine models of lung and renal cell carcinoma. *Clin. Cancer Res.* **23**, 5187–5201 (2017).
38. Shapiro, L. & Dinarello, C. A. Osmotic regulation of cytokine synthesis in vitro. *Proc. Natl Acad. Sci. USA* **92**, 12230–12234 (1995).
39. Han, J., Lee, J. D., Bibbs, L. & Ulevitch, R. J. A MAP kinase targeted by endotoxin and hyperosmolarity in mammalian cells. *Science* **265**, 808–811 (1994).
40. Machnik, A. et al. Macrophages regulate salt-dependent volume and blood pressure by a vascular endothelial growth factor-C-dependent buffering mechanism. *Nat. Med.* **15**, 545–552 (2009).
41. Wiig, H. et al. Immune cells control skin lymphatic electrolyte homeostasis and blood pressure. *J. Clin. Invest.* **123**, 2803–2815 (2013).
42. Machnik, A. et al. Mononuclear phagocyte system depletion blocks interstitial tonicity-responsive enhancer binding protein/vascular endothelial growth factor C expression and induces salt-sensitive hypertension in rats. *Hypertension* **55**, 755–761 (2010).
43. Go, W. Y., Liu, X., Roti, M. A., Liu, F. & Ho, S. N. NFAT5/TonEBP mutant mice define osmotic stress as a critical feature of the lymphoid microenvironment. *Proc. Natl Acad. Sci. USA* **101**, 10673–10678 (2004).
44. Kino, T. et al. Brx mediates the response of lymphocytes to osmotic stress through the activation of NFAT5. *Sci. Signal.* **2**, ra5 (2009).
45. Lanaspá, M. A. et al. High salt intake causes leptin resistance and obesity in mice by stimulating endogenous fructose production and metabolism. *Proc. Natl Acad. Sci. USA* **115**, 3138–3143 (2018).
46. Wilck, N. et al. Salt-responsive gut commensal modulates TH17 axis and disease. *Nature* **551**, 585–589 (2017).
47. O'Donnell, M. et al. Urinary sodium and potassium excretion, mortality, and cardiovascular events. *N. Engl. J. Med.* **371**, 612–623 (2014).
48. Minton, K. Antibacterial immunity: a pinch of salt. *Nat. Rev. Immunol.* **15**, 202 (2015).
49. Yang, L. et al. Expansion of myeloid immune suppressor Gr⁺CD11b⁺ cells in tumor-bearing host directly promotes tumor angiogenesis. *Cancer Cell* **6**, 409–421 (2004).
50. Gabrilovich, D. I., Ostrand-Rosenberg, S. & Bronte, V. Coordinated regulation of myeloid cells by tumours. *Nat. Rev. Immunol.* **12**, 253–268 (2012).
51. Franklin, R. A. et al. The cellular and molecular origin of tumor-associated macrophages. *Science* **344**, 921–925 (2014).
52. Zhou, J., Nefedova, Y., Lei, A. & Gabrilovich, D. Neutrophils and PMN-MDSC: their biological role and interaction with stromal cells. *Semin. Immunol.* **35**, 19–28 (2018).
53. Moses, K. & Brandau, S. Human neutrophils: their role in cancer and relation to myeloid-derived suppressor cells. *Semin. Immunol.* **28**, 187–196 (2016).
54. Wu, W. C. et al. Circulating hematopoietic stem and progenitor cells are myeloid-biased in cancer patients. *Proc. Natl Acad. Sci. USA* **111**, 4221–4226 (2014).
55. Veglia, F. et al. Fatty acid transport protein 2 reprograms neutrophils in cancer. *Nature* **569**, 73–78 (2019).
56. Zhang, W. C. et al. Elevated sodium chloride drives type I interferon signaling in macrophages and increases antiviral resistance. *J. Biol. Chem.* **293**, 1030–1039 (2018).
57. Serr, I. et al. A miRNA181a/NFAT5 axis links impaired T cell tolerance induction with autoimmune type 1 diabetes. *Sci. Transl. Med.* **10**, 1–14 (2018).
58. Yoon, H. J. et al. NF-AT5 is a critical regulator of inflammatory arthritis. *Arthritis Rheum.* **63**, 1843–1852 (2011).
59. Ohta, Y., Tsuchihashi, T., Kiyohara, K. & Oniki, H. High salt intake promotes a decline in renal function in hypertensive patients: a 10-year observational study. *Hypertens. Res.* **36**, 172–176 (2013).
60. Sjødahl, K. et al. Salt and gastric adenocarcinoma: a population-based cohort study in Norway. *Cancer Epidemiol. Biomark. Prev.* **17**, 1997–2001 (2008).
61. Kim, J., Park, S. & Nam, B. H. Gastric cancer and salt preference: a population-based cohort study in Korea. *Am. J. Clin. Nutr.* **91**, 1289–1293 (2010).
62. Lin, S. H., Li, Y. H., Leung, K., Huang, C. Y. & Wang, X. R. Salt processed food and gastric cancer in a Chinese population. *Asian Pac. J. Cancer Prev.* **15**, 5293–5298 (2014).
63. Zhang, W. C. et al. High salt primes a specific activation state of macrophages, M(Na). *Cell Res.* **25**, 893–910 (2015).
64. Yi, B. et al. Effects of dietary salt levels on monocytic cells and immune responses in healthy human subjects: a longitudinal study. *Transl. Res.* **166**, 103–110 (2015).
65. Sharma, P. & Allison, J. P. The future of immune checkpoint therapy. *Science* **348**, 56–61 (2015).
66. Wing, A. et al. Improving CART-Cell therapy of solid tumors with oncolytic virus-driven production of a bispecific T-cell engager. *Cancer Immunol. Res.* **6**, 605–616 (2018).
67. Tavazoei, M. F. et al. LXR/ApoE activation restricts innate immune suppression in cancer. *Cell* **172**, 825–840 e818 (2018).
68. Sica, A. & Massarotti, M. Myeloid suppressor cells in cancer and autoimmunity. *J. Autoimmun.* **85**, 117–125 (2017).
69. He, W. et al. Re-polarizing myeloid-derived suppressor cells (MDSCs) with cationic polymers for cancer immunotherapy. *Sci. Rep.* **6**, 24506 (2016).

Acknowledgements

This study was funded by the National Key Research and Development Programme of China (2017YFC0909702), the National Natural Science Foundation of China (81973273, 81673380, 31971309 and 31671031), the Jiangsu Province Funds for Distinguished Young Scientists (BK20170015) and the Fundamental Research Funds for the Central Universities (020814380115). C.W. acknowledges the funding support from the Science and Technology Development Fund, Macau SAR (FDCT No. 080/2016/A2, 0018/2019/AFJ, 0097/2019/A2) and the University of Macau (MYRG2017-00028-ICMS). L.D. acknowledges the UM Macau Distinguished Visiting Scholar (MDS) Programme. This study was also supported by the funds for the International Cooperation and Exchange of the Natural Science Foundation of China and the Science and Technology Development Fund (31961160701), Anhui provincial Natural Science Foundation (1908085QC131) and Grants for Scientific Research of BSKY (XJ201726) from Anhui Medical University.

Author contributions

W.H., L.D., C.W. and J.Z. conceived and designed the experiments; W.H., J.X., R.M. and Q.L. performed the experiments; W.H., J.X., D.L. and H.Z. analysed and interpreted the data; W.H., L.D., C.W. and J.Z. contributed to the preparation of the paper.

Competing interests

The authors declare no competing interests.

Additional information

Supplementary information is available for this paper at <https://doi.org/10.1038/s41467-020-15524-1>.

Correspondence and requests for materials should be addressed to J.Z., C.W. or L.D.

Peer review information *Nature Communications* thanks Jens Titze and the other, anonymous, reviewer(s) for their contribution to the peer review of this work. Peer reviewer reports are available.

Reprints and permission information is available at <http://www.nature.com/reprints>

Publisher's note Springer Nature remains neutral with regard to jurisdictional claims in published maps and institutional affiliations.



Open Access This article is licensed under a Creative Commons Attribution 4.0 International License, which permits use, sharing, adaptation, distribution and reproduction in any medium or format, as long as you give appropriate credit to the original author(s) and the source, provide a link to the Creative Commons license, and indicate if changes were made. The images or other third party material in this article are included in the article's Creative Commons license, unless indicated otherwise in a credit line to the material. If material is not included in the article's Creative Commons license and your intended use is not permitted by statutory regulation or exceeds the permitted use, you will need to obtain permission directly from the copyright holder. To view a copy of this license, visit <http://creativecommons.org/licenses/by/4.0/>.

© The Author(s) 2020